Results in Engineering 32 (2026) 112236

Contents lists available at ScienceDirect

Results in Engineering

journal homepage: www.sciencedirect.com/journal/results-in-engineering

Research paper

Deep-learning-based approach for accurate and rapid estimation of core body temperature using a single heat flux sensor

Hankyung Kim [a,1], Chuljin Hwang [a,b,1], Dae Yu Kim [a,b,c,*]

[a] Department of Electrical and Computer Engineering, Inha University, Incheon, 22212, Republic of Korea
[b] Center for Sensor Systems, Inha University, Incheon, 22212, Republic of Korea
[c] Inha Research Institute for Aerospace Medicine, Inha University, Incheon, 22212, Republic of Korea

ARTICLE INFO

Keywords:
Core body temperature prediction
Single heat flux sensor
Transient thermal response
Deep learning model
Environmental robustness

ABSTRACT

Accurate and rapid prediction of core body temperature (CBT) is essential for monitoring physiological homeostasis, enabling early detection of fever, thermal stress, and circulatory dysfunction. Wearable CBT sensors were required to provide reliable measurements under diverse environmental conditions to support continuous health monitoring and clinical decision-making. However, real-time CBT prediction without prolonged thermal stabilization and while maintaining robustness against environmental interferences remained a significant challenge. This paper introduced a concentric cylindrical single heat-flux sensor integrated with a deep-learning framework that was trained on a large dataset including finite-element simulation results and experimentally validated transient thermal responses. A developed deep learning model that learned conduction- and convection-governed features from only the initial 30 s of temperature signals achieved a mean absolute error below 0.1°C across various boundary conditions at ambient temperature (5–35°C), convective heat transfer coefficients (0–50 W·m^{-2}·K^{-1}), skin thermal conductivity (0.32–0.50 W·m^{-1}·K^{-1}) and sensor thickness (1–5 mm). The framework demonstrated rapid convergence, sustained accuracy under airflow perturbations, as well as reliable tracking during 75 min of stepwise CBT variations. Validation with skin-mimicking phantoms further confirmed robustness of the developed model across environmental and physiological conditions. The proposed approach collectively enabled noninvasive and site-independent real-time CBT monitoring and provided strong potential for continuous health surveillance, early fever diagnosis, and thermal stress assessment.

1. Introduction

Core body temperature (CBT) is a fundamental physiological parameter, alongside heart rate, blood pressure, and blood oxygen saturation [1–5]. As a direct reflection of endogenous heat production from cellular metabolism and thermoregulatory processes, CBT provided critical insights into systemic physiological status and abnormal thermal responses [6,7]. Skin temperature is strongly influenced by ambient conditions while CBT remained stable and provided an accurate representation of the internal thermal state [8]. Therefore, continuous and precise monitoring of CBT is essential for early detection of hyperthermia in infectious diseases as well as for assessing thermal strain in individuals exposed to extreme environments [9–13]. According to ISO 9886:2004, CBT could be directly assessed at various anatomical sites, including the esophagus [14,15], oral cavity [16], rectum [17,18], tympanic membrane [19,20], external auditory canal [21], and urine [22]. These methods are widely used in clinical and laboratory settings although they are unsuitable for real-world monitoring owing to their invasiveness and their tendency to interfere with daily activities and safety concerns as well as high cost and poor user compliance [23,24]. These limitations highlight the need for non-invasive and user-friendly alternatives enabling reliable CBT assessment in real-world settings [25].

Various non-invasive approaches have been developed, including in-ear sensors, infrared thermography, ingestible telemetric capsules, and heat-flux-based wearable devices [26]. Each technique presents inherent trade-offs in accuracy, invasiveness, wearability, and robustness to environmental and physiological variability. In-ear sensors are sensitive to anatomical placement and ambient conditions, whereas ingestible capsules are constrained by single-use operation, ingestion

* Corresponding author.
E-mail address: dyukim@inha.ac.kr (D.Y. Kim).
[1] These authors contributed equally

https://doi.org/10.1016/j.rineng.2026.112236
Received 13 January 2026; Received in revised form 1 June 2026; Accepted 27 July 2026
Available online 27 July 2026

burden, and limited monitoring duration. To overcome these limitations, the zero-heat-flux (ZHF) technique has been widely investigated as a representative method for estimating CBT.

The ZHF method offers a non-invasive and physiologically interpretable approach, in which an insulating layer was actively heated until no net heat transfer occurs between the skin and environment, thereby achieving thermal equilibrium [27–30]. For example, Mäkinen et al. [31] evaluated the clinical performance of a commercial ZHF system (SpotOn; 3M, St. Paul, MN) in patients undergoing vascular and cardiac surgeries. Good agreement was noted between the ZHF-based forehead temperature and conventional CBT measurements, with mean biases of +0.08°C relative to esophageal temperature during vascular surgery and –0.05°C relative to pulmonary artery temperature in cardiac surgery. Despite this accuracy, ZHF sensors require extended equilibration periods and remain susceptible to environmental perturbations (e.g., ambient temperature and airflow), which limit their responsiveness to rapid CBT fluctuations [32]. Furthermore, the continuous operation of integrated heating elements entails substantial power consumption, constraining their suitability for long-term wearable applications [33].

To surpass the constraints of ZHF methods, single heat-flux–based approaches have been actively investigated as passive low-power alternatives. Several strategies have been proposed to improve the environmental robustness of equation-based single heat-flux estimation. For example, Hashimoto et al. introduced a time-derivative compensation term combined with a high-conductivity probe cover to suppress lateral heat loss, achieving estimation errors within 0.076°C under controlled airflow conditions [34]. In parallel, calibration-free techniques based on numerical simulation datasets have been proposed to reduce reliance on empirical calibration by leveraging precomputed thermal responses under various conditions [35,36]. Although these approaches improve robustness under controlled environments, they remained dependent on predefined estimation equations and require prior knowledge of site-specific thermal parameters, limiting their adaptability across diverse environmental and physiological conditions.

In this study, a single heat-flux-based sensor was integrated with a deep-learning framework for valid and rapid CBT estimation. This sensor employed a concentric cylindrical polydimethylsiloxane (PDMS)/polyethylene (PE) foam structure that suppressed lateral heat dissipation and promoted axial heat transfer, enabled the stable acquisition of transient temperature signals between the skin and the ambient environment. The deep-learning network was implemented as a convolutional–recurrent architecture that processed transient response signals acquired from the top and bottom thermistors. Unlike conventional equation-based approached relying on steady-state assumptions, the proposed convolutional 1D–gated recurrent unit (Conv1D–GRU) model directly learned thermal responses. Convolutional layers extracted local response features, while recurrent layers captured temporal dependencies in signal dynamics, enabling robust prediction under varying conditions. By learning complex thermal responses beyond the capability of equation-based methods, the proposed model achieved high prediction accuracy with fast convergence, reducing the error to less than 0.1°C within only 30 s of measurement. For practical implementation, a concentric cylindrical structure was adopted for the thermal conduction layer, which enhanced directional heat transfer and suppressed convective effects.

Comprehensive numerical simulations and experiments demonstrated that the single heat-flux-based sensor integrated with the deep-learning framework enabled reliable CBT prediction under diverse environmental and geometric conditions. Furthermore, validation across different anatomical sites, including the forehead, chest, and wrist, demonstrated site-independent accuracy, with the predicted CBT consistently within 0.2°C of the axillary reference. Overall, this study highlighted the potential of combining heat-flux sensing with a deep-learning framework to overcome the limitations of equation-based estimation and ZHF methods, thereby enabling real-time, site-independent CBT monitoring.

2. Materials and methods

2.1. Materials and reagents

PDMS was prepared using a SYLGARD™ 184 Silicone Elastomer Kit (base and curing agent), purchased from Dow Corning Co. Ltd. (Shanghai, China). Ethylene propylene diene monomer (EPDM) rubber (thickness of 10 mm) [37], selected for its thermal conductivity similar to that of human skin, was purchased from Kumho Polychem Co. Ltd. (Republic of Korea). Thermistors (NTC 10K 3950) were purchased from China.

2.2. Finite-element modeling of the heat-flux sensor

Numerical simulations of the single heat-flux sensor were performed using the *Heat Transfer in Solids* module in COMSOL Multiphysics 5.4 (Stockholm, Sweden) [32,38]. A two-dimensional cross-sectional geometry was constructed based on the actual dimensions of the fabricated device (Fig. S1). The computational domain was discretized using a physics-controlled mesh, with maximum and minimum element sizes of 4 and 0.5 mm, respectively. Mesh independence and solver convergence were verified across three physics-controlled mesh configurations (maximum/minimum element sizes: 2.75/0.2, 4/0.5, and 5/0.72 mm). The mean temperature differences across all three mesh configurations were 0.024 ± 0.038°C and 0.011 ± 0.020°C at the top and bottom sensor surfaces, respectively (Fig. S2A). Adaptive time stepping was employed, with all three configurations converging to a maximum time step of 150 s (Fig. S2B). The relative residual norms decreased to the order of 10^{-5} within three iterations for all configurations, confirming solver convergence (Fig. S2C). Transient simulations employed a time step of 1.2 s over a total duration of 1,200 s. The governing equations in both models were solved using the PARDISO direct solver. Thermophysical properties of the constituent materials were defined based on reported values [39]. The skin domain was modeled with a fixed thickness of 5 mm, and the basal boundary was set to a CBT (T_{core}) of 37.5°C [38].

2.3. Heat-flux-based CBT estimation

Heat transfer within the human body could be described using Pennes' bioheat equation [40], which balances heat conduction, blood perfusion, and metabolic heat generation:

$$\rho c\frac{\partial T}{\partial t} = k\nabla^2 T + \rho_b\omega_b c_b(T_b - T) + Q_m \quad (1)$$

where ρ was the tissue density (kg·m^{-3}), c was the specific heat of tissue (J·kg^{-1}·K^{-1}), and $\partial T/\partial t$ represents the transient change in tissue temperature with time; k denoted the thermal conductivity of tissue (W·m^{-1}·K^{-1}), and $\nabla^2 T$ accounts for heat conduction by spatial diffusion; ρ_b was the density of blood (kg·m^{-3}); ω_b was the blood perfusion rate per unit volume of tissue (s^{-1}), c_b was the specific heat of blood (J·kg^{-1}·K^{-1}), and (T_b – T) denoted the convective heat exchange between blood and tissue; and Q_m represented the metabolic heat generation rate per unit volume (W·m^{-3}). Eq. (1) explained how internal heat was conducted outward through tissue and exchanged with blood flow [41]. To measure this internal heat at the skin surface, a sensor had to detect the temperature gradient formed as heat travels from the core toward the environment.

The single heat-flux method estimated CBT using two thermistors placed within the sensor structure. The bottom thermistor, located close to the skin, mainly reflected conduction-driven heat transfer, while the top thermistor, exposed to the ambient air, responded strongly to changes in the environment. From one-dimensional steady-state heat conduction analysis, the CBT can be estimated as [42]

$$\mathrm{T_{core-esti}} \approx \mathrm{T_{bottom}} + \frac{\mathrm{k_s}}{\mathrm{k_g}}\left(\mathrm{T_{bottom}} - \mathrm{T_{top}}\right) \quad (2)$$

where $T_{\text{core-esti}}$ denoted the CBT estimated using the equation-based method; T_{bottom} and T_{top} denoted the temperatures measured at the skin-facing and ambient-facing thermistors, respectively; and k_s and k_g represented the thermal conductivity of the sensor and tissue, respectively. Eq. (2) showed that T_{core} can be approximated from the net heat flux [43].

2.4. Deep-learning architecture for transient CBT prediction

The Conv1D–GRU network was designed to predict CBT from transient thermal responses recorded by the sensor. The top and bottom thermistor signals were min–max normalized and sequentially processed through convolutional layers that extracted local thermal gradients, followed by GRU units that captured long-range temporal dependencies. A fully connected regression head continuously estimated CBT. Model optimization employed the Adam algorithm with mini-batch updates, and the initial learning rate was selected from a predefined search space. Training was performed for up to 200 epochs, with early stopping applied once the validation loss stopped improving. A weighted mean-squared error function was adopted to strongly penalize small deviations near thermal equilibrium. Hyperparameters —including convolutional filter size and number, GRU unit count, dense layer width, and learning rate—were systematically tuned, and the final configuration is summarized in Table S1. The dataset was randomly partitioned into training, validation, and test sets at an 8:1:1 ratio. All computations were executed in TensorFlow with GPU acceleration.

2.5. Sensor fabrication

The single heat-flux sensor was designed with a concentric cylindrical structure composed of an inner PDMS core and an outer PE foam shell. The PDMS component (diameter 10 mm; height 4.5 mm) was manually molded and centrally positioned to function as the primary thermal conduit between the internal heat source and skin–contact interface. A surrounding PE foam layer with a thickness of 5 mm was concentrically assembled around the PDMS core. The foam was precisely machined to conform to the outer geometry of the device and included embedded cavities to integrate electronic components. Owing to its low thermal conductivity, the PE layer functioned as an effective thermal insulator, minimizing lateral and convective heat loss while enhancing directional heat transfer toward the skin surface.

2.6. Experimental evaluation under controlled conditions

The fabricated sensor was evaluated on a laboratory hotplate serving as a controlled heat source. The plate temperature was adjusted to simulate reference CBT values in the range of 36–38°C. An EPDM rubber sheet was placed between the hotplate and sensor to mimic the thermal properties of skin. To assess the influence of convective cooling, a fan was positioned vertically above the sensor, and airflow velocity was monitored using a vane anemometer (Testo SE & Co. KGaA, Lenzkirch, Germany) that provided a measurement range of 0.4–30 m/s and an accuracy of ±0.2 m/s.

2.7. Thermistor calibration

The thermal response of the fabricated single heat-flux sensor was evaluated in a temperature-controlled environment using a drying oven and refrigerator. Electrical resistance was recorded using a USB-Temp data acquisition module (Measurement Computing, USA) at 16-bit resolution and a sampling rate of 1 Hz. For each setpoint the temperature was maintained for at least 7 min and resistance was measured at least three times to obtain the mean. The thermistors were calibrated by fitting the resistance–temperature relationship with the Steinhart–Hart equation, which provided an empirical representation of the nonlinear dependence of thermistor resistance on temperature [44]:

$$\frac{1}{T} = A + B(\ln R) + C(\ln R)^3 \quad (3)$$

where T was the absolute temperature (K); A, B, and C were Steinhart–Hart coefficients determined from calibration data; and R was the measured resistance (Ω). The MF55 NTC thermistors employed in the present prototype had a nominal resistance of 10 kΩ at 25°C, a B value of 3950 K, and a resistance tolerance of 1%, corresponding to a temperature measurement uncertainty of approximately ±0.24°C in the operating range of 30–38°C. Given that a voltage divider circuit measured the resistance, the effective temperature resolution was 0.01°C, which was sufficient to capture the thermal gradients required to estimate CBT. The thermistor-level uncertainty was compensated through the Steinhart–Hart calibration procedure, and the calibrated accuracy was verified to be within ±0.1°C, consistent with the ASTM E1112 criterion.

3. Results and discussion

3.1. Boundary condition effects on CBT estimation

Accurate CBT prediction required explicit consideration of heat transfer between the body and surrounding environment, as boundary conditions including ambient temperature (T_{air}) and convective heat transfer coefficient (h) strongly affect the temperature measured at the skin surface. Moreover, geometric factors including the thickness of the skin-equivalent layer influence heat transport across the sensor–skin interface and can affect estimation accuracy. To evaluate these effects and optimize heat flux–based estimation strategies, numerical modeling was performed using COMSOL Multiphysics. The computational geometry was constructed as a concentric cylindrical model representing the single heat-flux sensor (Fig. 1A). The structure consisted of an inner core (diameter of 10 mm) and outer shell (diameter of 30 mm, height of 5 mm).

Finite-element simulations were performed to investigate the impact of variations in boundary properties, including ambient conditions, tissue conductivity, and sensor geometry, on CBT estimation error. As shown in Fig. 1B, increasing the ambient temperature (T_{air}) from 20 to 36°C reduced the estimation error from 0.67 to 0.06°C. At lower T_{air}, the large temperature gap between the skin and environment caused a significant drop in T_{top}, generating an abnormally large ΔT ($T_{\text{bottom}-\text{ top}}$) that distorted the estimation in Eq. (2) and increased error. As T_{air} increased, surface cooling was hindered, ΔT decreased to a physiologically realistic range, and $T_{\text{core-esti}}$ converged toward the true T_{core}.

In contrast, variations in h produced the opposite effect (Fig. 1C). With h near zero, T_{top} approached T_{bottom} owing to minimal airflow, resulting in an insufficient ΔT that provided little corrective input to Eq. (2), yielding an error of 0.83°C. As h increased to 50 W/m²·K, T_{top} decreased while T_{bottom} remained nearly constant, enlarging ΔT to a useful range that enabled accurate estimation and reduced the error to 0.52°C. This trend reflected the assumption implicit in Eq. (2) that convective resistance at the top surface was negligible, such that $T_{\text{top}} = T_{\text{air}}$. In practice, a finite convective resistance elevates T_{top} above T_{air}, reducing ΔT below the assumed value and introducing underestimation error. As h increased, this resistance decreased, and T_{top} approached T_{air}, progressively satisfying the assumption and reducing error. In the present concentric cylindrical design, surface-integrated heat fluxes at the bottom (q_{skin}) and top (q_{top}) of the PDMS core were extracted from steady-state COMSOL simulations with h swept from 0 to 50 $\text{W}\cdot\text{m}^{-2}\cdot\text{K}^{-1}$ to quantify the heat loss fraction, defined as $(q_{\text{skin}} - q_{\text{top}})/q_{\text{skin}}$. As shown in Fig. S3, both q_{skin} and q_{top} increased monotonically with h, while the heat loss fraction decreased from ~100% at $h = 0$ to 28.1% at $h = 50$

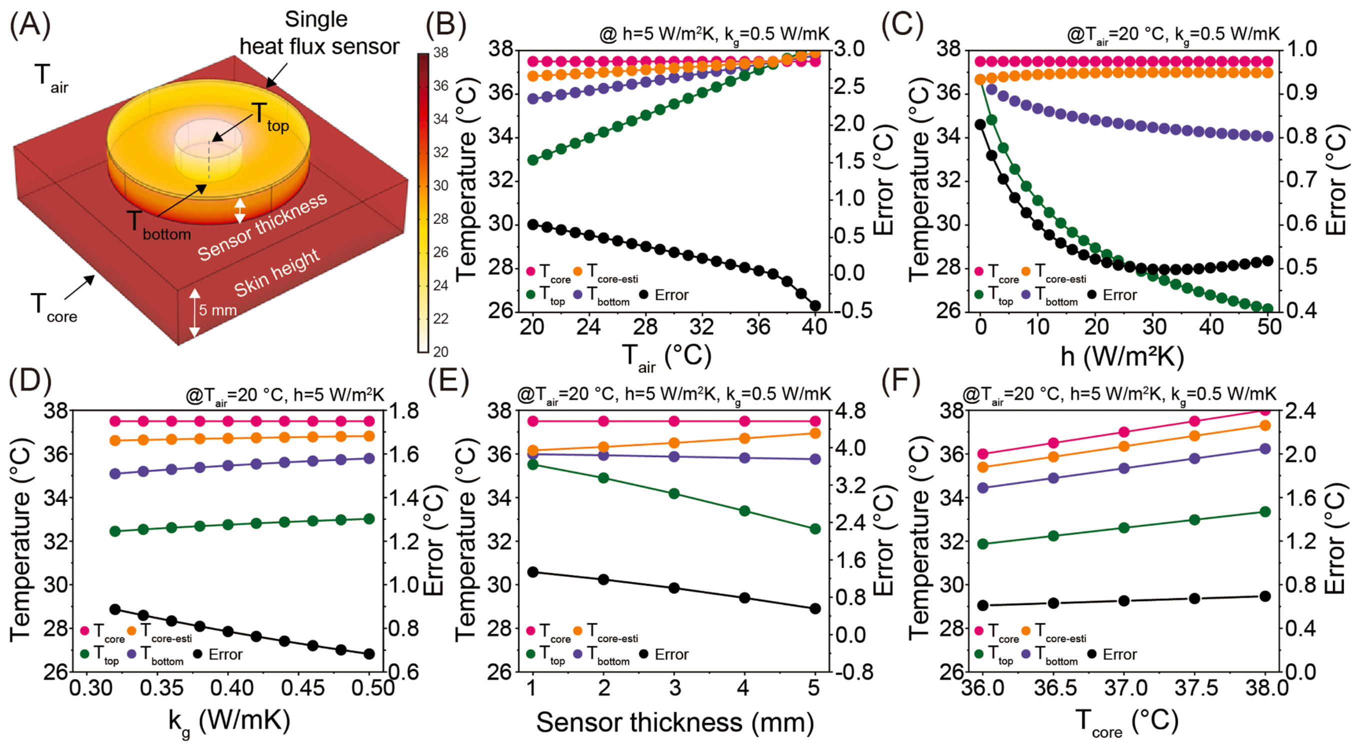

Fig. 1. COMSOL Multiphysics simulation results of a concentric cylinder-type heat-flux sensor for core body temperature (CBT) estimation. (A) Schematic of the axisymmetric concentric cylinder geometry, consisting of a central thermal conduction core and surrounding insulation layers. Parametric analysis of CBT estimation under varying conditions: (B) Estimated CBT as a function of T_{air}, (C) convective heat transfer coefficient (h), (D) skin thermal conductivity (k_g), (E) sensor thickness, and (F) reference core temperature (T_{core}).

W·m^{-2}·K^{-1}. Beyond environmental effects, skin thermal conductivity also influenced estimation accuracy. As shown in Fig. 1D, increasing k_g from 0.32 to 0.50 W m^{-1}·K^{-1} reduced the error from 0.89 to 0.68°C. Higher skin conductivity enhanced heat conduction from the core to the surface, reduced variations in ΔT, and thereby decreased estimation error in Eq. (2). Geometric characteristics of the sensor further influenced prediction accuracy. As shown in Fig. 1E, increasing the thickness from 1 to 5 mm reduced the error from 1.34 to 0.56°C. Thin sensors allowed ambient perturbations to propagate to T_{bottom}, collapsing ΔT and generating error. Increasing thickness preserved ΔT within an appropriate range, improving the compensation in Eq. (2). Nevertheless, further increase in thickness inevitably enlarges device bulk, presenting a practical limitation for wearable applications. The effect of the total sensor diameter on the estimation accuracy was examined through additional finite element method (FEM) simulations in which total sensor diameter was varied from 20 to 60 mm while keeping the PDMS core diameter fixed at 10 mm (Fig. S4). The estimation error decreased from 0.956°C at 20 mm to 0.652°C at 60 mm, reflecting how the thicker PE foam suppressed lateral heat dissipation and better preserved the one-dimensional heat flow assumption of Eq. (2). Notably, the error reduction became minimally beyond 30 mm, indicating saturation. Finally, Fig. 1F shows that varying T_{core} from 36.0 to 38.0°C increased the estimation error from 0.61 to 0.69°C, respectively. The number of errors with T_{core} increased because the increase in ΔT did not scale proportionally with T_{core}. Under fixed boundary conditions, a 0.5°C increase in T_{core} increased T_{bottom} and T_{top} by 0.449 and 0.369°C, respectively, yielding a ΔT increment of only 0.080°C. This limited increase in ΔT was insufficient to fully compensate for the change in T_{core} in Eq. (2), thus progressively increasing the estimation error.

Collectively, the simulation results showed that CBT estimation error arises from the combined influence of environmental factors (T_{air} and h) and intrinsic properties (k_g, T_{core}, and sensor thickness) that govern heat transfer across the body–sensor interface. Environmental variations primarily altered sensor surface temperatures, whereas conductivity and geometry modulated the efficiency of heat transport from the core to the skin. Absolute CBT value also contributed to estimation error, producing persistent deviations of approximately 0.6°C under fixed boundary conditions, although boundary variations induced even larger errors. These findings underscored the limitations of fixed equation-based methods and motivated the development of data-driven correction frameworks capable of incorporating boundary-dependent variability.

3.2. Conv1D–GRU model performance and comparative benchmarking

Fig. 2A schematically illustrated the CBT prediction framework. The input data included T_{top} and T_{bottom} signals generated from 92,820 environmental conditions, including variations in T_{air}, h, and k_g. Parameter ranges and the corresponding transient responses within a fixed 30 s window were summarized in Fig. S5, and the corresponding ambient-temperature-dependent estimation error under the baseline condition was provided in Fig. S6. To determine the input window length, two independent criteria were considered: an accuracy threshold and a latency constraint. The former follows ASTM E1112, which mandates a ±0.1°C tolerance within the physiological range near 37°C, governing the minimum window length. The latency constraint defined its maximum, as excessively long windows introduced response delays incompatible with real-time wearable monitoring. The optimal window length thus resided at the intersection of these two bounds. Although cumulative loss appeared to converge by ~15 s (Fig. S7), window-length analysis showed that the mean absolute error (MAE) fell below 0.1°C only for windows ≥ 30 s (Fig. S8). The 30 s window was therefore selected as a practical upper bound to ensure the ±0.1°C accuracy requirement while remaining compatible with continuous real-time monitoring and minimizing latency.

Accordingly, the input window was fixed at 30 s to satisfy the ±0.1°C criterion while minimizing latency. Each sequence was normalized by

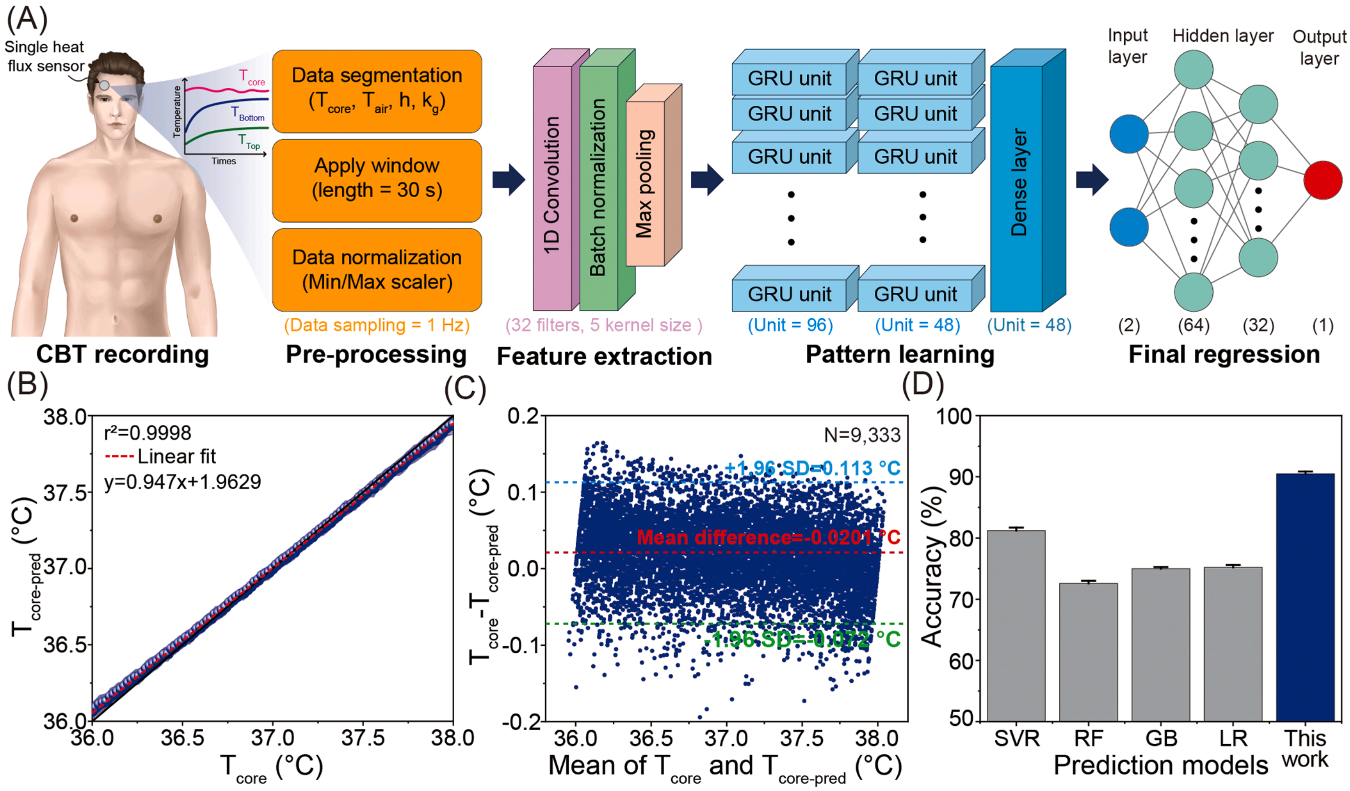

Fig. 2. Deep-learning-based framework for non-invasive CBT prediction and performance evaluation (A) Schematic workflow of the CBT prediction algorithm using a single heat-flux sensor. Transient and steady-state temperature signals were segmented and normalized, followed by feature extraction and sequential pattern learning through stacked GRU layers, with final regression yielding T_{core} estimates. (B) Correlation between predicted CBT ($T_{core\text{-}pred}$) and reference CBT (T_{core}) within 36–38°C. The dashed red line indicates linear regression (slope = 0.947, r^2 = 0.9998), and error bars represent standard deviations of binned data. (C) Bland–Altman plot comparing $T_{core\text{-}pred}$ and T_{core} (N = 9,333), showing a mean bias of –0.0201°C with limits of agreement from –0.072°C to +0.113°C. (D) Bar plots of CBT prediction accuracy (%) for support vector regression (SVR), random forest (RF), gradient boosting (GB), linear regression (LR), and the GRU-based model. Bars indicate mean accuracy values within ±0.1°C, and error bars denote standard deviations across cross-validation folds. All models used identical inputs and preprocessing steps (T_{top}, T_{bottom}, T_{air}, h, k_g; 30-s windows at 1 Hz).

min–max scaling to preserve the temporal profile within a uniform range. Feature extraction was performed using one-dimensional convolution with 32 filters (kernel size = 5) to detect local gradients in the transient temperature profile, followed by batch normalization and max pooling to stabilize feature distribution and retain dominant patterns. The processed features were then propagated through stacked GRU layers: The first GRU (96 units) captured global temporal dynamics, while the subsequent GRUs (48 units each) refined intermediate and short-range dependencies. In the regression stage, dense layers with 64 and 32 hidden units integrated the temporal features into a single CBT output. Auxiliary supervision with steady-state temperature was applied at intermediate layers to improve feature representation, generalization, and training stability. This architecture, combining Conv1D and GRU modules, enabled simultaneous extraction of local thermal gradients and sequential dynamics, thereby achieving robust CBT prediction from 30 s transient responses.

Fig. 2B shows that predicted CBT ($T_{core\text{-}pred}$) aligned closely with the reference CBT (T_{core}) across the physiological range of 36–38°C, exhibiting a regression slope near unity with minimal scatter. Correlation analysis yielded a coefficient of determination $r^2 > 0.99$ (N = 9,333), indicating high accuracy. To further evaluate agreement beyond correlation, Bland–Altman analysis was performed (Fig. 2C). The comparison between $T_{core\text{-}pred}$ and T_{core} showed a negligible mean bias of –0.0201°C, with 95% limits of agreement from +0.113 to –0.072°C. Nearly all data points fell within the limits of agreement, indicating strong concordance across the physiological range.

For comparative benchmarking, the Conv1D–GRU architecture was assessed alongside representative algorithms frequently employed in prior CBT prediction studies, including support vector regression (SVR), random forest (RF), gradient boosting (GB), and linear regression (LR) (Fig. 2D). Prediction accuracy was defined as the proportion of cases with $|T_{core\text{-}pred} - T_{core}| < 0.1$°C, which was consistent with clinical thermometer standards. Conv1D–GRU achieved 95.17% accuracy, higher than those of SVR (81.2 %), RF (72.6 %), GB (75 %), and LR (75.2 %). Bland–Altman plots for each model, illustrating error distributions and agreement with reference CBT, are provided in Fig. S9. The observed performance gap is attributable to differences in handling time-dependent information: SVR cannot effectively capture sequential dependencies, RF produces discretization errors due to its piecewise-constant regression scheme, and GB tends to propagate residual noise during sequential fitting. LR also exhibited limited accuracy because its linear mapping could not capture the nonlinear thermal interactions or the transient dynamics embedded in T_{top} and T_{bottom} signals. In contrast, the Conv1D–GRU combines convolutional layers for local gradient detection with recurrent layers for sequential dependency modeling, enabling more reliable CBT estimation. Beyond comparisons with conventional machine-learning models, Table S2 provided a summary of estimation accuracy reported in prior CBT sensing studies, highlighting the superior prediction accuracy of the present framework.

3.3. Experimental validation under controlled conditions

After establishing predictive feasibility through FEM and deep-learning training, experimental validation was performed to evaluate the T_{core} prediction accuracy. The experimental setup provided controlled thermal and convective conditions (Fig. 3A), including a

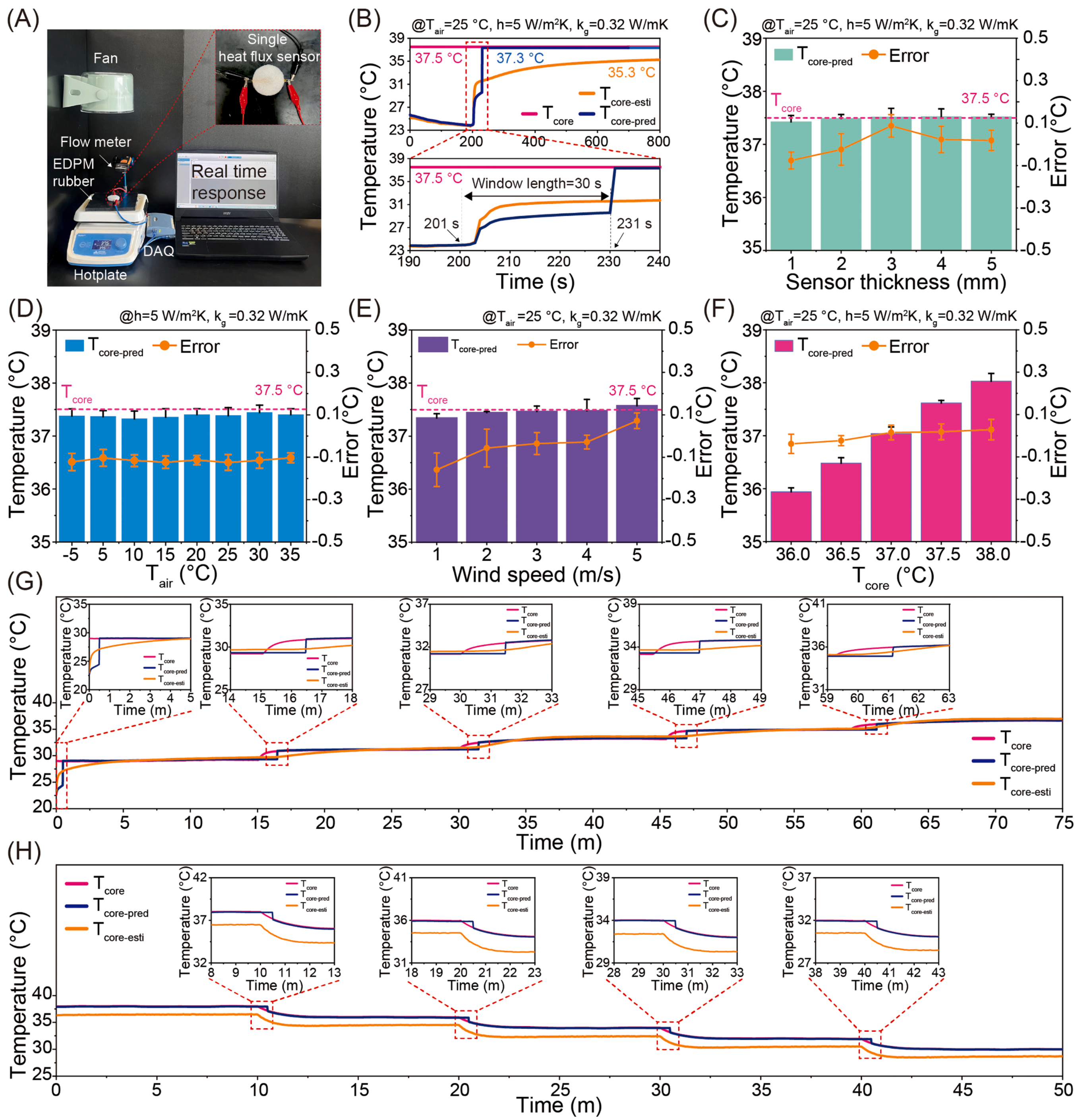

Fig. 3. CBT measurement under different environmental and sensor parameters. (A) Photograph of the experimental setup consisting of a hotplate, flow meter, fan, and data acquisition (DAQ) system connected to the single heat-flux sensor. (B) Representative temperature response showing reference temperature (T_{core}), CBT predicted by the deep-learning model ($T_{core\text{-}pred}$), and equation-based estimate ($T_{core\text{-}esti}$). The inset shows the initial convergence period, where $T_{core\text{-}pred}$ rapidly approached the reference within 30 s (33.72°C vs. 33.75°C). In contrast, $T_{core\text{-}esti}$ increased slowly and failed to reach the reference within the measurement period. Effects of key parameters on CBT prediction, with reference T_{core} of 37.5°C (C) sensor thickness (1–5 mm), (D) ambient temperature (T_{air} = 5–35°C), and (E) wind speed (1–5 m·s^{-1}). (F) Effect of T_{core} (36.0–38.0°C) on CBT prediction. $T_{core\text{-}pred}$ increased in parallel with the reference T_{core}, and the corresponding errors were within ±0.3°C. EPDM rubber with a thermal conductivity of k_g = 0.32 W·m^{-1}·K^{-1} was used as the skin surrogate. (G) Dynamic evaluation of CBT prediction under stepwise changes in reference temperature. The hotplate was increased every 15 min over a 75 min period. $T_{core\text{-}pred}$ (blue) rapidly converged to each temperature level within 30 s, while $T_{core\text{-}esti}$ (orange) showed delayed responses. Figure insets show transient responses during transitions: $T_{core\text{-}pred}$ adjusted promptly to new temperature levels compared with the slower response of $T_{core\text{-}esti}$. Dynamic evaluation of CBT prediction during a stepwise (G) increased and (H) decreased in the reference temperature. $T_{core\text{-}pred}$ (blue) rapidly converged to each temperature level, whereas $T_{core\text{-}esti}$ (orange) showed delayed responses. The figure insets showed transient responses during transitions: $T_{core\text{-}pred}$ adjusted more promptly to new temperature levels than $T_{core\text{-}esti}$.

temperature-regulated hotplate as a stable heat source, fan with a flowmeter to modulate airflow, and single heat-flux sensor coupled to a real-time data acquisition unit for continuous signal recording. The sensor was designed in a concentric cylindrical configuration, consisting of a PDMS thermal conductor positioned between top and bottom thermistors and encapsulated with a PE foam layer (thickness of 0.5 mm at the top and 30 mm at the lateral sides) for thermal insulation. This architecture facilitated directional heat transfer toward the sensing elements while minimizing environmental perturbations, thereby improving prediction robustness under variable test conditions. To ensure reproducibility, the hotplate surface temperature was pre-calibrated and validated using infrared thermography.

Fig. 3B presents the time-course response of the single heat-flux sensor, comparing $T_{\text{core-pred}}$ with the conventional equation-based estimate ($T_{\text{core-esti}}$). $T_{\text{core-pred}}$ converged to the reference T_{core} within 30 s, reaching 37.34°C by 231 s with a deviation of less than 0.2°C from the true value (37.5°C). Thereafter, $T_{\text{core-pred}}$ maintained close agreement with the reference throughout the observation window. In contrast, $T_{\text{core-esti}}$ exhibited markedly slower dynamics, reaching only 35.3°C at 800 s—more than 2°C below the reference—and failing to reach equilibrium within the experimental timeframe. This deviation was attributable to the limitation of the equation-based model, which relied solely on steady-state heat conduction and thus converges slowly under transient boundary conditions. In contrast, $T_{\text{core-pred}}$ captures both the transient gradients and sequential thermal patterns from the input signals, enabling rapid adaptation and accurate alignment with the reference T_{core}.

Figs. 3C–F summarized the effects of sensor geometry, environmental fluctuations, and physiological variation on prediction accuracy. Across thicknesses of 1–5 mm, $T_{\text{core-pred}}$ consistently tracked the reference within ±0.2°C, with the 5-mm configuration yielding the lowest error (0.00177 ± 0.0581°C), consistent with simulations predicting enhanced thermal stability at this dimension. Under environmental fluctuations, $T_{\text{core-pred}}$ remained within ±0.2°C across ambient temperatures of -5–35°C (Fig. 3D). To quantify the influence of airflow, wind speed was translated into h through the Nusselt relation ($Nu = hL/k$, Fig. S10). According to the laminar boundary-layer correlation, h increased from 0 to ~50 $W{\cdot}m^{-2}{\cdot}K^{-1}$ as wind speed rose from 0 to 5 $m{\cdot}s^{-1}$. Within this range, $T_{\text{core-pred}}$ maintained errors below ±0.3°C (Fig. 3E), demonstrating robust prediction under convective conditions. Furthermore, under horizontal airflow, $T_{\text{core-pred}}$ exhibited similarly low error and stable behavior across wind speeds of 1–5 m s^{-1} (Fig. S11), indicating robustness to both the airflow magnitude and direction. When the reference T_{core} varied from 36.0 to 38.0°C to mimic physiological fluctuation, $T_{\text{core-pred}}$ increased proportionally with the reference and maintained errors below ±0.3°C (Fig. 3F). Under stepwise changes in T_{core}, $T_{\text{core-pred}}$ rapidly and stably tracked both increasing and decreasing transitions (Fig. 3G–H), reaching each new temperature level within 30 s with minimal deviation under transient conditions. Collectively, these results demonstrate that the framework preserves high accuracy under

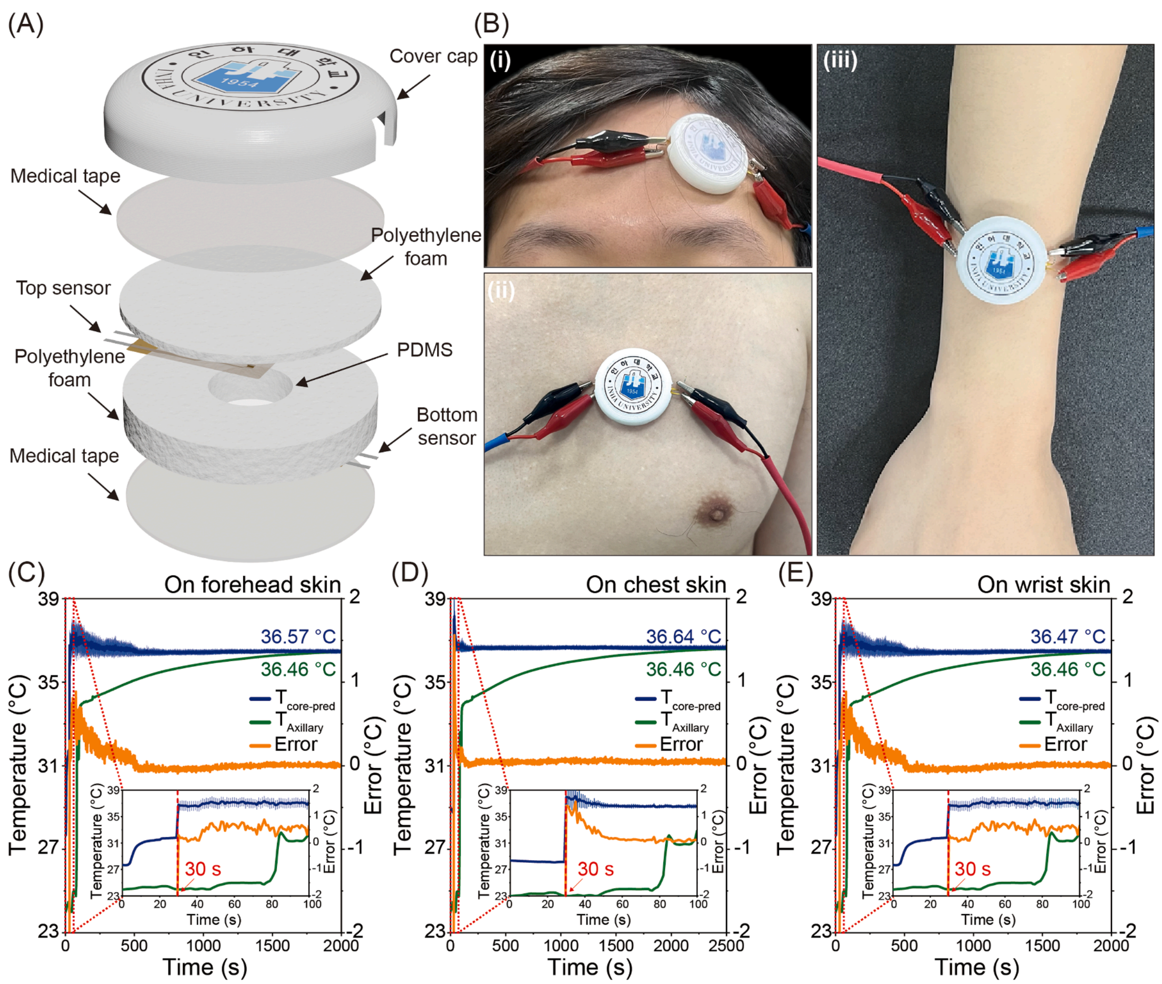

Fig. 4. Design and validation of a single heat-flux-based CBT sensor across different anatomical sites. (A) Schematic of the concentric cylindrical heat-flux-based CBT sensor, including a PDMS thermal conductor, embedded temperature sensors, and PE foam insulator, encapsulated with medical tape and a cover cap. (B) Photographs of sensor attachment on the (i) forehead, (ii) chest, and (iii) wrist. Estimated CBT (blue) compared with axillary reference (green) at forehead (C), chest (D), and wrist (E). Estimation error is plotted in orange. Figure insets present enlarged plots of the initial 100 s, highlighting sensor response stabilization within 30 s.

varying boundary conditions and within physiologically relevant CBT ranges.

3.4. In vivo CBT monitoring across anatomical sites

The feasibility of CBT estimation using the single heat-flux-based temperature sensor was demonstrated. The device was designed with a concentric cylindrical structure, consisting of a PDMS thermal conductor surrounded by PE foam insulation, and encapsulated with medical tape and a protective cover (Fig. 4A). The sensor was conformally mounted on different anatomical sites, including the forehead, chest, and wrist (Fig. 4B), using medical tape, which enabled stable attachment without causing discomfort or requiring additional fixation. During the experiments, the sensor continuously monitored CBT at the applied sites for approximately 2 h, while an axillary temperature patch provided synchronous reference measurements(T_{axillary}). Although pulmonary artery or rectal temperatures serve as the clinical gold standard, axillary measurement was selected as a practical, non-invasive surrogate for prolonged monitoring in conscious subjects. This setup enabled the evaluation of deep-learning-based CBT estimation under varying k_g, verifying that the proposed approach could provide reliable predictions independent of anatomical site.

As shown in Figs. 4C–E, the deep-learning model successfully reproduced CBT dynamics across all anatomical sites and converged to consistent predictions within 30 s. The insets highlighted the fast response of the proposed sensor–model framework, with the temperature error decreasing to less than $\pm 0.2^\circ$C within 30 s, which was essential for capturing dynamic changes in CBT during real-time monitoring. At steady state, the estimated CBT values at the forehead ($T_{\text{core-pred}} = 36.57^\circ$C and $T_{\text{axillary}} = 36.46^\circ$C), chest ($T_{\text{core-pred}} = 36.64^\circ$C and $T_{\text{axillary}} = 36.46^\circ$C), and wrist ($T_{\text{core-pred}} = 36.47^\circ$C and $T_{\text{axillary}}=36.46^\circ$C) remained within 0.2°C of the axillary reference, demonstrating high accuracy across different anatomical sites. The agreement observed at the wrist was attained under controlled indoor conditions with stable peripheral perfusion. Collectively, these results indicated that the single heat-flux-based sensor integrated with a deep-learning model enabled reliable, site-independent, and continuous CBT monitoring with clinically relevant response times.

3.5. Limitations

Despite the promising capability of the single heat-flux-based sensor integrated with a deep-learning model for reliable, site-independent, and continuous CBT monitoring, this study faced several limitations that should be acknowledged. First, the numerical model assumed a spatially uniform convective heat transfer coefficient across the probe surface, whereas in practical deployment, directional airflow induced by subject movement or environmental conditions generated spatially non-uniform convection. This discrepancy introduced spatial variations in heat transfer, potentially affecting estimation accuracy. Second, axillary temperature was used as the in vivo reference in place of invasive gold-standard measures. Although thermoneutral resting conditions minimized the axillary-to-core temperature offset, a residual discrepancy remained, which could have affected the absolute accuracy of the reference. Finally, this method was validated in vivo under thermally neutral indoor resting conditions. Under cold stress or vigorous exercise, vasoconstriction could introduce a tissue-level thermal offset, and the results reported herein should not be directly extrapolated to such physiologically demanding scenarios. In addition, environmental and physiological factors, including solar radiation and variations in blood perfusion, were not explicitly considered, which can influence heat transfer at the skin–sensor interface. In order to surpass constraints, future work will focus on developing a hybrid modeling framework that integrates physics-based thermal modeling with data-driven learning, enabling the incorporation of additional factors such as evaporative heat transfer, spatially non-uniform convection, and physiological variability.

4. Conclusions

In this study, we developed a deep-learning framework integrated with a single heat-flux sensor for valid and rapid estimation of CBT. Finite-element simulations and controlled experiments demonstrated that the model maintained a mean absolute error below 0.1°C under variations in ambient temperature, convective heat transfer, skin conductivity, and sensor geometry. By extracting transient thermal features, the convolutional–recurrent network achieved rapid convergence to accurate values within 30 s for real-time applications and substantially faster than equilibrium-based methods. The integrated sensor–model framework provided consistent accuracy under airflow disturbances, environmental fluctuations, prolonged monitoring periods, and across multiple anatomical sites in vivo. Collectively, these findings underscored the potential of combining heat-flux sensing with data-driven learning to enable non-invasive, site-independent, and real-time CBT monitoring, with direct implications for continuous health surveillance, early fever detection, and thermal stress evaluation.

Funding sources

This work was supported by the Korea Institute for Advancement of Technology (KIAT) grant funded by the Korea Government (MOTIE) (RS-2022-KI002581, HRD Program for Industrial Innovation), by the Korea Medical Device Development Fund grant funded by the Korea government (the Ministry of Science and ICT, the Ministry of Trade, Industry and Energy, the Ministry of Health & Welfare, the Ministry of Food and Drug Safety) (RS-2023-00242778), by the National Research Foundation of Korea (NRF) grant funded by the Korea Government (MSIT) (RS-2025-00559359), and by the BK21 FOUR Program funded by the Ministry of Education (MOE, Korea) and the National Research Foundation of Korea (NRF).

Declaration of ethics

All procedures involving human subjects were conducted in accordance with the Declaration of Helsinki and applicable institutional guidelines. Ethical approval for this study was obtained from the Inha University Institutional Review Board (IRB approval no. 250804-1AR3). The participant was informed of the study purpose, measurement procedure, and use of the collected temperature data, and provided informed consent prior to participation.

CRediT authorship contribution statement

Hankyung Kim: Writing – original draft, Investigation, Formal analysis. **Chuljin Hwang:** Writing – original draft, Investigation, Formal analysis. **Dae Yu Kim:** Writing – review & editing, Project administration.

Declaration of competing interest

The authors declare that they have no known competing financial interests or personal relationships that could have appeared to influence the work reported in this paper.

Supplementary materials

Supplementary material associated with this article can be found, in the online version, at doi:10.1016/j.rineng.2026.112236.

Data availability

Data will be made available on request.

References

[1] X. Ren, C. Zhou, X. Ye, A novel miniaturized sandwich-like sensor for continuous measurement of core body temperature, IEEE Sens. J. 22 (17) (2022) 16742–16749, https://doi.org/10.1109/JSEN.2021.3071825.

[2] J. Wu, Z. Hu, Z. Han, Y. Gu, L. Yang, B. Sun, Human physiological responses of exposure to extremely cold environments, J. Therm. Biol. 98 (2021) 102933, https://doi.org/10.1016/j.jtherbio.2021.102933.

[3] A. Zavareh, B. Tran, C. Orred, S. Rhodes, M.S. Rahman, M. Namkoong, R. Lee, C. Carlisle, M. Rosas, A. Pavlov, I. Chen, G. Schilling, M. Smith, F. Masood, J. Hanks, L. Tian, Soft wearable thermal devices integrated with machine learning, Adv. Mater. Technol. 8 (16) (2023) 2300206, https://doi.org/10.1002/admt.202300206.

[4] *Diurnal rhythms of wrist temperature are associated with future disease risk in the UK Biobank | Nature Communications*. https://www.nature.com/articles/s41467-023-40977-5 (accessed 2025-09-02).

[5] Q. Hua, J. Sun, H. Liu, R. Bao, R. Yu, J. Zhai, C. Pan, Z.L. Wang, Skin-inspired highly stretchable and conformable matrix networks for multifunctional sensing, Nat. Commun. 9 (1) (2018) 244, https://doi.org/10.1038/s41467-017-02685-9.

[6] M.-G. Kang, H.-R. Kim, H.Y. Lee, C. Kwak, H. Koh, B.H. Kang, J.-S. Roe, H.-W. Rhee, Mitochondrial thermogenesis can trigger heat shock response in the nucleus, ACS Cent. Sci. 10 (6) (2024) 1231–1241, https://doi.org/10.1021/acscentsci.3c01589.

[7] E. Rivas, M. Rao, T. Castleberry, V. Ben-Ezra, The change in metabolic heat production is a primary mediator of heat acclimation in adults, J. Therm. Biol. 70 (2017) 69–79, https://doi.org/10.1016/j.jtherbio.2017.10.001.

[8] A. Chen, J. Zhu, Q. Lin, W. Liu, A comparative study of forehead temperature and core body temperature under varying ambient temperature conditions, Int. J. Environ. Res. Public Health 19 (23) (2022) 15883, https://doi.org/10.3390/ijerph192315883.

[9] P.L. Rajbhandary, G. Nallathambi, Feasibility of continuous monitoring of core body temperature using chest-worn patch sensor, Annu. Int. Conf. IEEE Eng. Med. Biol. Soc. 2020 (2020) 4652–4655, https://doi.org/10.1109/EMBC44109.2020.9175579.

[10] G. Liu, Y. Zhang, L. Tang, Research progress in core body temperature measurement during target temperature management, J. Integr. Nurs. 4 (1) (2022) 36–41, https://doi.org/10.4103/jin.jin_40_21.

[11] *Wireless, multimodal sensors for continuous measurement of pressure, temperature, and hydration of patients in wheelchair | npj Flexible Electronics*. https://www.nature.com/articles/s41528-023-00238-3 (accessed 2025-09-02).

[12] Y. Jin, G. Chen, K. Lao, S. Li, Y. Lu, Y. Gan, Z. Li, J. Hu, J. Huang, J. Wen, H. Deng, M. Yang, Z. Chen, X. Hu, B. Liang, J. Luo, Identifying human body states by using a flexible integrated sensor, npj Flex Electron. 4 (1) (2020) 28, https://doi.org/10.1038/s41528-020-00090-9.

[13] *Battery-free, wireless sensors for full-body pressure and temperature mapping | Science Translational Medicine*. https://www.science.org/doi/10.1126/scitranslmed.aan4950 (accessed 2025-09-02).

[14] A.J. Kadado, J.G. Akar, J.P. Hummel, Luminal esophageal temperature monitoring to reduce esophageal thermal injury during catheter ablation for atrial fibrillation: a review, Trends Cardiovasc. Med. 29 (5) (2019) 264–271, https://doi.org/10.1016/j.tcm.2018.09.010.

[15] A. Salihu, H. Lu, N. Maurizi, G. Tzimas, C. Herrera Siklody, M. Le Bloa, G. Domenichini, C. Teres, S. Hugelshofer, P. Monney, E. Pruvot, O. Muller, P. Antiochos, P. Pascale, Prevention of esophageal lesions during atrial fibrillation catheter ablation using esophageal temperature monitoring: a systematic review and meta-analysis, Pacing. Clin. Electrophysiol. 47 (5) (2024) 614–625, https://doi.org/10.1111/pace.14972.

[16] S.M. Mazerolle, M.S. Ganio, D.J. Casa, J. Vingren, J. Klau, Is oral temperature an accurate measurement of deep body temperature? a systematic review, J. Athl. Train. 46 (5) (2011) 566–573, https://doi.org/10.4085/1062-6050-46.5.566.

[17] K.E. Boehm, K.C. Miller, Does gender affect rectal temperature cooling rates? a critically appraised topic, J. Sport Rehabil. 28 (5) (2019) 522–525, https://doi.org/10.1123/jsr.2018-0081.

[18] D. Kardum, E.F. Bell, B.F. Grčić, A. Müller, Duration of skin-to-skin care and rectal temperatures in late preterm and term infants, BMC Pregnancy Childbirth 22 (1) (2022) 655, https://doi.org/10.1186/s12884-022-04983-7.

[19] Y.-H. Kim, H.-J. Park, J.-H. Yoo, Effect of eardrum perforation and chronic otitis media on the results of infrared tympanic thermometer in adults: a systematic review and meta-analysis, Medicine 102 (45) (2023) e35932, https://doi.org/10.1097/MD.0000000000035932.

[20] P.W. McCarthy, A.I. Heusch, The vagaries of ear temperature assessment, J. Med. Eng. Technol. 30 (4) (2006) 242–251, https://doi.org/10.1080/03091900600711415.

[21] *Continuous core body temperature monitoring for heatstroke alert via a wearable in-ear thermometer | ACS Sensors*. https://pubs.acs.org/doi/10.1021/acssensors.4c03470 (accessed 2025-09-02).

[22] Standard, I. 9886, Ergonomics-Evaluation of Thermal Strain by Physiological Measurements, Second Edition, International Standard Organization, 2004, pp. 1–21.

[23] N. Verdel, T. Podlogar, U. Ciuha, H.-C. Holmberg, T. Debevec, M. Supej, Reliability and validity of the core sensor to assess core body temperature during cycling exercise, Sensors 21 (17) (2021) 5932, https://doi.org/10.3390/s21175932.

[24] D.S. Moran, L. Mendal, Core temperature measurement: methods and current insights, Sports Med. 32 (14) (2002) 879–885, https://doi.org/10.2165/00007256-200232140-00001.

[25] A. Eisenkraft, N. Goldstein, M. Fons, M. Tabi, A.D. Sherman, A. Ben Ishay, R. Merin, D. Nachman, Comparing body temperature measurements using the double sensor method within a wearable device with oral and core body temperature measurements using medical grade thermometers—a short report, Front. Physiol. 14 (2023) 1279314, https://doi.org/10.3389/fphys.2023.1279314.

[26] Y. Hashimoto, A comprehensive review of non-invasive core body temperature measurement techniques, Sensors 26 (3) (2026) 972, https://doi.org/10.3390/s26030972.

[27] H. Liang, J.-Y. Wang, Y. Liang, X.-F. Shao, Y.-L. Ding, H.-Q. Jia, Agreement of zero-heat-flux thermometry with the oesophageal and tympanic core temperature measurement in patient receiving major surgery, J. Clin. Monit. Comput. 38 (1) (2024) 197–203, https://doi.org/10.1007/s10877-023-01078-2.

[28] C. Pedersen, P. Munch, J. Kjaergaard, L. Grønlykke, A. Bräuer, Accuracy of a zero-heat-flux thermometer in cardiac surgery, a prospective, multicentre, method comparison study, Sci. Rep. 14 (1) (2024) 3169, https://doi.org/10.1038/s41598-024-53647-3.

[29] H. Aksu Erdost, S. Özkardeşler, A.K. Değirmenci, R.M. Dalak, C. Terzi, Intraoperative temperature monitoring with zero heat flux technology (3M SpotOn Sensor) in comparison with tympanic and oesophageal temperature and hypotermia risk factors: an observational study, Turk. J. Anaesthesiol. Reanim. 49 (2) (2021) 100–106, https://doi.org/10.5152/TJAR.2020.33.

[30] D. Hart, M. Rischall, K. Durgin, M. Donoghue, T. Pham, T. Wyatt, J. Stang, P. DeVries, B. Driver, Non-invasive zero-heat-flux technology compared with traditional core temperature measurements in the emergency department, Am. J. Emerg. Med. 38 (11) (2020) 2383–2386, https://doi.org/10.1016/j.ajem.2020.08.071.

[31] M.-T. Mäkinen, A. Pesonen, I. Jousela, J. Päivärinta, S. Poikajärvi, A. Albäck, U.-S. Salminen, E. Pesonen, Novel zero-heat-flux deep body temperature measurement in lower extremity vascular and cardiac surgery, J. Cardiothorac. Vasc. Anesth. 30 (4) (2016) 973–978, https://doi.org/10.1053/j.jvca.2016.03.141.

[32] H. Lu, S. Aratake, H. Naito, M. Nogawa, T. Nemoto, T. Togawa, S. Tanaka, Development of a core body thermometer applicable for high-temperature environment based on the zero-heat-flux method, Sensors 23 (4) (2023) 1970, https://doi.org/10.3390/s23041970.

[33] L.P.J. Teunissen, J. Klewer, A. De Haan, J.J. De Koning, H.A.M. Daanen, Non-invasive continuous core temperature measurement by zero heat flux, Physiol. Meas. 32 (5) (2011) 559–570, https://doi.org/10.1088/0967-3334/32/5/005.

[34] Y. Hashimoto, S. Tada, Y. Nishida, Improvement of environmental robustness in non-invasive core body temperature sensor studied numerically and experimentally, Sens. Actuators A: Phys. 368 (2024) 115136, https://doi.org/10.1016/j.sna.2024.115136.

[35] Y. Hashimoto, S. Tada, Y. Nishida, Reference-free calibration for wearable core body temperature sensor based on single-heat-flux method, IEEE Sens. Lett. 8 (9) (2024) 1–4, https://doi.org/10.1109/LSENS.2024.3435965.

[36] Y. Hashimoto, S. Tada, Y. Nishida, Rapid dataset-free self-calibration for heat flux-based core body temperature sensors, IEEE Access 13 (2025) 61048–61055, https://doi.org/10.1109/ACCESS.2025.3556405.

[37] Y. Tanaka, D. Matsunaga, T. Tajima, M. Seyama, Robust skin attachable sensor for core body temperature monitoring, IEEE Sens. J. 21 (14) (2021) 16118–16123, https://doi.org/10.1109/JSEN.2021.3075864.

[38] Y. Du, C. Zhou, Y. Feng, L.Flexible Qiu, Multimodal device for measurement of body temperature, core temperature, thermal conductivity and water content, npj Flex Electron. 8 (1) (2024) 85, https://doi.org/10.1038/s41528-024-00373-5.

[39] D.V. Akulova, M.A. Sheremet, Mathematical simulation of bio-heat transfer in tissues having five layers in the presence of a tumor zone, Mathematics 12 (5) (2024) 676, https://doi.org/10.3390/math12050676.

[40] T.-C. Shih, P. Yuan, W.-L. Lin, H.-S. Kou, Analytical analysis of the Pennes bioheat transfer equation with sinusoidal heat flux condition on skin surface, Med. Eng. Phys. 29 (9) (2007) 946–953, https://doi.org/10.1016/j.medengphy.2006.10.008.

[41] J. Hristov, Bio-heat models revisited: concepts, derivations, nondimensalization and fractionalization approaches, Front. Phys. 7 (2019), https://doi.org/10.3389/fphy.2019.00189.

[42] D. Janke, N. Kagelmann, C. Storm, M.A. Maggioni, C. Kienast, H.-C. Gunga, O. Opatz, Measuring core body temperature using a non-invasive, disposable double-sensor during targeted temperature management in post-cardiac arrest patients, Front. Med. 8 (2021) 666908, https://doi.org/10.3389/fmed.2021.666908.

[43] L. Atallah, C. Ciuhu, I. Paulussen, E. Bongers, A.H.M. Blom, A. Idrissi, G. Noordergraaf, Perioperative measurement of core body temperature using an unobtrusive passive heat flow sensor, J. Clin. Monit. Comput. 34 (6) (2020) 1351–1359, https://doi.org/10.1007/s10877-019-00446-1.

[44] Fraden, J. Handbook of Modern Sensors: Physics, Designs, and Applications, Fourth Edition.